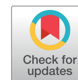

Boron–oxygen complex yields n-type surface layer in semiconducting diamond

Xiaobing Liu[a,b,1], Xin Chen[a,b,1], David J. Singh[c], Richard A. Stern[d], Jinsong Wu[e], Sylvain Petitgirard[f], Craig R. Bina[b], and Steven D. Jacobsen[b,1]

[a]School of Physics and Physical Engineering, Qufu Normal University, Qufu, 273165 Shandong, China; [b]Department of Earth and Planetary Sciences, Northwestern University, Evanston, IL 60208; [c]Department of Physics and Astronomy, University of Missouri, Columbia, MO 65211; [d]Canadian Centre for Isotopic Microanalysis, Department of Earth and Atmospheric Sciences, University of Alberta, Edmonton, AB T6G 2E3, Canada; [e]Northwestern University Atomic and Nanoscale Characterization Experimental, Northwestern University, Evanston, IL 60208; and [f]Bayerisches Geoinstitut, University of Bayreuth, 95444 Bayreuth, Germany

Edited by Ho-kwang Mao, Carnegie Institution for Science, Washington, DC, and approved March 5, 2019 (received for review December 19, 2018)

Diamond is a wide-bandgap semiconductor possessing exceptional physical and chemical properties with the potential to miniaturize high-power electronics. Whereas boron-doped diamond (BDD) is a well-known p-type semiconductor, fabrication of practical diamond-based electronic devices awaits development of an effective n-type dopant with satisfactory electrical properties. Here we report the synthesis of n-type diamond, containing boron (B) and oxygen (O) complex defects. We obtain high carrier concentration (~0.778 × 10^{21} cm^{-3}) several orders of magnitude greater than previously obtained with sulfur or phosphorous, accompanied by high electrical conductivity. In high-pressure high-temperature (HPHT) boron-doped diamond single crystal we formed a boron-rich layer ~1–1.5 μm thick in the {111} surface containing up to 1.4 atomic % B. We show that under certain HPHT conditions the boron dopants combine with oxygen defects to form B–O complexes that can be tuned by controlling the experimental parameters for diamond crystallization, thus giving rise to n-type conduction. First-principles calculations indicate that B_3O and B_4O complexes with low formation energies exhibit shallow donor levels, elucidating the mechanism of the n-type semiconducting behavior.

diamond | boron | defects | semiconductor | high pressure

The wide bandgap (~5.47 eV) and extreme thermal-mechanical properties of diamond make it a potentially transformative material for future electronic and optoelectronic devices for high-power, wide-frequency, and high-temperature applications (1). Due to its extreme stiffness, diamond-based transistors could operate under high mechanical stresses, while also possessing high thermal conductivity (~14 times greater than silicon), chemical inertness, biocompatibility, and high drift mobility for electrons and holes (4,500 and 3,800 $cm^2\ V^{-1}\ s^{-1}$) at room temperature (2, 3). Diamond also has an exceptionally high dielectric breakdown strength ~30 times higher than silicon, which combined with its high thermal conductivity and resistance to radiation damage makes it an ideal semiconductor for miniaturizing transistors in high-power applications such as in automobiles and spacecraft (3, 4). Furthermore, diamond fabricated as an n-type semiconductor with suitable surface treatment may also be a negative electron affinity material (5). Whereas boron (B) is a well-known p-type dopant in diamond serving as a charge acceptor, n-type doping in diamond remains an outstanding challenge in materials science (6).

Several group 15 (Va) or 16 (VIa) elements (nitrogen, phosphorus, and sulfur) have been investigated as potential electron donors to obtain n-type diamond (7–9). Nitrogen, the dominant impurity in most natural and synthetic diamond, was expected to be a shallow donor by analogy to substitutional phosphorus (P_{sub}) in silicon. However, N_{sub} dopants in diamond behave as deep donors with an energy (E_d) ~1.7 eV below the conduction band minimum (E_{CBM}) (10). Furthermore, diamond containing aggregated N atoms (A-center, B-center, etc.) is fairly insulating, limiting N to act as an efficient donor (8, 11). Sulfur has also been predicted to form shallow donor states ($E_d \sim E_{CBM} - 0.38$ eV) (9, 12); however, the electronic characteristics of S-doped diamond with low carrier content (~10^{12}–10^{16} cm^{-3}) are inadequate for most devices (13). P_{sub} has emerged as the most successful n-type dopant in diamond ($E_d \sim E_{CBM} - 0.5$ eV) (1, 14, 15). However, phosphorus donors are relatively inefficient with low carrier concentration (below 10^{19} cm^{-3}), low conductivity (below $10^{-4}\ \Omega^{-1}\ cm^{-1}$), and low electron mobility (below 250 $cm^2\ V^{-1}\ s^{-1}$) in diamond (14, 16). These challenges have been attributed to the formation of complexes with C vacancies related to high formation energy (10.4 eV) during diamond crystallization, the high ionization energy (0.6 eV) of phosphorus in diamond, and/or the presence of growth-related defects in the {111} epilayers. Thus, a suitable n-type dopant with satisfactory carrier concentration and mobility remains an outstanding challenge for future diamond-based electronic applications.

Theoretical and experimental studies have suggested complex defects (N–H–N, or B–deuterium) in diamond could produce shallow donor states (17–19). A conversion of p-type to n-type behavior was reported in homoepitaxial deuterated boron-doped diamond (BDD) layers (18), and the existence of B–D_2 complexes generates n-type behavior with good electrical conductivity

APPLIED PHYSICAL SCIENCES

Significance

Diamond is a uniquely attractive wide-bandgap semiconductor for future electronic devices where its remarkable physical properties may enable switches, transistors, and diodes for extreme applications. Whereas p-type semiconducting diamond is well developed with boron doping, the synthesis of n-type diamond, required to complete purely diamond-based electronics, has been a great challenge in materials science. We report the creation of n-type diamond via a new type of defect complexes of boron and oxygen that can be tuned by controlling the experimental parameters for diamond crystallization, leading to a shallow donor state with high carrier concentration that is several orders of magnitude higher than achieved by sulfur or phosphorus doping. The results provide a new strategy for producing n-type diamond-based devices.

Author contributions: X.L. and X.C. designed research; X.L., X.C., R.A.S., and J.W. performed research; X.L., R.A.S., J.W., and S.P. contributed new reagents/analytic tools; X.L., X.C., D.J.S., R.A.S., J.W., C.R.B., and S.D.J. analyzed data; and X.L., X.C., C.R.B., and S.D.J. wrote the paper.

The authors declare no conflict of interest.

This article is a PNAS Direct Submission.

This open access article is distributed under Creative Commons Attribution-NonCommercial-NoDerivatives License 4.0 (CC BY-NC-ND).

[1]To whom correspondence may be addressed. Email: xiaobing.phy@qfnu.edu.cn, chenxin@qfnu.edu.cn, or s-jacobsen@northwestern.edu.

This article contains supporting information online at www.pnas.org/lookup/suppl/doi:10.1073/pnas.1821612116/-/DCSupplemental.

Published online April 1, 2019.

after exposing BDD to deuterium plasma for 8 h at 520 °C. However, this route is problematic because thermal deuteration treatments decrease the conductivity and sometimes convert the diamond back to p-type. Here we report the creation of n-type semiconducting diamond through complex defects of B and O. The atomic ratio of B and O in the B–O complexes can be tuned by controlling experimental P–T parameters for diamond crystallization. Synthesis of high-quality single-crystal diamond (~7.5 mm in longest dimension) heavily doped with B and O in the {111} surface provides the basis for definitive characterization. Our synthesis route creates a strategy for producing n-type diamond.

To synthesize single-crystal BDD, high-purity graphite powders (99.99 wt % purity) and amorphous boron (99.999 wt % purity) were used as carbon and boron sources through the temperature gradient growth (TGG) method under high-pressure and high-temperature (HPHT) conditions in a China-type cubic high-pressure apparatus (*SI Appendix*, Fig. S1 and Table S1). Aluminum (1.0 wt %) and titanium (0.5 wt %) were added to the starting materials as nitrogen sinks. We adjusted the boron content for diamond crystallization by changing the ratio of amorphous boron in the NiMnCo catalyst (0.5, 1.0, 1.5, 2.0, 2.5, 3.0, and 3.5 wt % B across all runs). We controlled the P–T conditions for diamond synthesis at 5.5–5.8 GPa and temperatures ranging from 1,620 to 1,740 K. Long run times up to 75 h were employed to grow large diamonds. A summary of P–T conditions and sample identification numbers for various BDD grown in this study are presented in Tables 1 and 2 and *SI Appendix*, Table S1. Fig. 1*A* shows the effect of boron on the growth rate of single-crystal diamond under HPHT conditions. We found that the growth rate of diamond decreased with increasing percentage of boron added to the catalyst, whereas the growth rate was enhanced by increasing reaction temperatures. At relatively low reaction temperatures (below 1,660 K with 2.5–3.5 wt % B additive), formation of cracks or aggregates of diamond crystals were obtained, and both nucleation and growth of diamond were completely terminated below 1,628 K. Higher-quality crystals were achieved at reaction temperatures approaching 1,740 K.

By adding boron to the system, the {100} growth surfaces tend to disappear, and the {111} direction exhibits the most stable growth form of diamond with boron above 1.0 wt %. All produced BDD single crystals are black in color and opaque. High quality single-crystal diamond was produced on {100} substrate (Fig. 1*B*; ~5.5 mm in longest dimension) and {111} substrate (Fig. 1*C*; ~7.5 mm in longest dimension) at 1,685 K with 3.0 wt % B additive before cutting and polishing. Fig. 1 *D* and *E* show the typical defects observed on the {111} faces of BDD samples (sample BDD-F is shown). The diamond surface is composed of thin platelets with diameters ranging from 10 to 120 μm. A representative plate-like structure ~150 nm in thickness is shown in Fig. 1*F*. Scanning electron microscopy (SEM) shows the detailed microstructure of these thin platelets formed during diamond growth (*SI Appendix*, Fig. S2), indicating the nucleation and extension of tiny diamond crystallites across the diamond substrate. The individual crystallites are well aligned on the {111} surfaces and eventually merge to form a thin film of single-crystal diamond.

Raman spectroscopy was used to study the chemical nature of the {111} surfaces of BDD samples synthesized at 1,660–1,730 K (*SI Appendix*, Fig. S3*A*). Raman spectra of the boron-related impurity in diamond produced at 1,660 K (samples A–F in *SI Appendix*, Table S1) are dominated by two broad bands at about 300–700 and 900–1,250 cm^{-1}, which arise and increase with increasing boron addition. Vibrational spectra of the first-order longitudinal phonon in BDD shift to lower frequency with increasing B, from 1,332.5 cm^{-1} for sample BDD-A with 0.5 wt % B to 1,327.0 cm^{-1} for sample BDD-F with 3.0 wt % B. In addition, the FWHM broadens from 4.6 cm^{-1} (BDD-A) to 14.0 cm^{-1} (BDD-F) (*SI Appendix*, Fig. S3) due to the increasing tensile stress with increasing B content in diamond and/or effect of Fano line shape in heavily doped diamond. Homogeneity of the impurity distribution on the as-grown {111} surface is illustrated by Raman spectroscopy mapping (*SI Appendix*, Fig. S3). With increasing reaction temperature, the boron dopant exhibits significantly different states in the BDD samples (*SI Appendix*, Fig. S4). Fig. 2 shows Raman spectra of BDD samples grown at 1,730 K (sample BDD-I) and 1,660 K (BDD-F) with 3.0 wt % B additive. Although the spectra for BDD-F exhibit the well-known peaks for BDD with heavy boron doping (dominated by broad features at 477 and 1,222.3 cm^{-1}) (20), sample BDD-I shows new peaks at 602, 880, 938, 1,048, 1,162, 1,225, and 1,466 cm^{-1}.

We further characterized the states of impurities in samples BDD-I and BDD-F using X-ray photoelectron spectroscopy (XPS) analysis of B 1*s*, C 1*s*, and O 1*s* (Fig. 2*C*). The B 1*s* scans reveal that the chemical environments of boron dopants on the

Table 1. Synthesis conditions (pressure P, temperature T, and time t), sample names and run numbers (in parentheses), and results of SIMS, XPS, and Hall effect measurements of BDD single crystals produced in this study; diamond {111} surface, as-grown state

Sample names and synthesis conditions	B content (cm^{-3}) (SIMS)	B states (XPS)	Hall effect results
Sample-F (Z15022530-17)	1.9–2.6 × 10^{21}	B–C: 73.7 (±0.1)%	ρ = 0.022 Ω·cm
P = 5.6 GPa		B–O: 26.3 (±0.1)%	R_H = −1.286 × 10^{-2} m^3/C
T = 1,660 K			n = 0.778 × 10^{21} cm^{-3}
t = 30 h			μ_n = 0.58 cm^2 V^{-1} s^{-1}
Sample-G (Z15022027-15)	1.7–2.4 × 10^{21}	B–C: 67.6 (±0.1)%	ρ = 0.137 Ω·cm
P = 5.6 GPa		B–O: 32.4 (±0.1)%	R_H = −2.076 × 10^{-2} m^3/C
T = 1,685 K			n = 0.301 × 10^{21} cm^{-3}
t = 27 h			μ_n = 0.15 cm^2 V^{-1} s^{-1}
Sample-H (Z15021823-12)	1.6–2.1 × 10^{21}	B–C: 51.7 (±0.1)%	ρ = 0.247 Ω·cm
P = 5.6 GPa		B–O: 48.3 (±0.1)%	R_H = 1.095 × 10^{-2} m^3/C
T = 1,710 K			p = 0.570 × 10^{21} cm^{-3}
t = 23 h			μ_n = 0.04 cm^2 V^{-1} s^{-1}
Sample-I (Z15021524-10)	1.4–2.0 × 10^{21}	B–C: 44.8 (±0.1)%	ρ = 0.231 Ω·cm
P = 5.6 GPa		B–O: 55.2 (±0.1)%	R_H = 2.310 × 10^{-2} m^3/C
T = 1,730 K			p = 0.271 × 10^{21} cm^{-3}
t = 24 h			μ_n = 0.10 cm^2 V^{-1} s^{-1}

μ_n, carrier mobility; ρ, electrical resistivity; n, carrier concentration; R_H, Hall coefficient.

Table 2. Results of SIMS and Hall effect measurements of BDD single crystals produced in this study

Sample names	B content (cm^{-3}) (SIMS)	Hall effect results
Sample-f	$1.5–2.1 \times 10^{20}$	$\rho = 0.239$ Ω·cm $R_H = 0.983\ m^3/C$ $p = 3.276 \times 10^{18}\ cm^{-3}$ $\mu_n = 4.11\ cm^2\ V^{-1}\ s^{-1}$
Sample-g	$1.4–1.9 \times 10^{20}$	$\rho = 7.165$ Ω·cm $R_H = 462.027\ m^3/C$ $p = 1.351 \times 10^{16}\ cm^{-3}$ $\mu_n = 64.48\ cm^2\ V^{-1}\ s^{-1}$
Sample-h	$1.3–1.8 \times 10^{20}$	$\rho = 0.228$ Ω·cm $R_H = 1.905\ m^3/C$ $p = 1.195 \times 10^{19}\ cm^{-3}$ $\mu_n = 8.36\ cm^2\ V^{-1}\ s^{-1}$
Sample-i	$1.1–1.7 \times 10^{20}$	$\rho = 0.509$ Ω·cm $R_H = 0.522\ m^3/C$ $p = 1.195 \times 10^{19}\ cm^{-3}$ $\mu_n = 1.03\ cm^2\ V^{-1}\ s^{-1}$

Sample names with lowercase letters (diamond interior, after removing B-rich surface layer) refer to the same samples in Table 1 with uppercase letters (before removing surface layer). μ_n, carrier mobility; ρ, electrical resistivity; n, carrier concentration; R_H, Hall coefficient.

as-grown BDD {111} surfaces of samples BDD-I (1,730 K) and BDD-F (1,660 K) are distinctly different. The B 1*s* region of the spectra for both samples is fitted with three peaks, located at 186.5, 188.6, and 192.7 eV, corresponding to B–C and B–O bonds in the diamond structure (21–23). This suggests that B–C and B–O are the primary interactions for B in the boron-rich surface layers of these BDD samples. The positions corresponding to B–C are similar to those for B–C in B_4C and BC_3 (24, 25). The small peak at 188.6 eV is very close to that of B 1*s* (188.4 eV) in h-BNC film (21), corresponding to a contribution from sp^2 bonding configurations (π^*) of B and C. In addition, although the C 1*s* spectrum shown in Fig. 2*D* is dominated by the peak at 285.2 eV, a small shoulder at 283.2 eV is also present and consistent with π^* observed in h-BNC film. Thus, sp^2 bonding configurations of B contribute to the Raman peak at 1,521.6 cm^{-1} in heavily B-doped diamond (*SI Appendix*, Fig. S3*A*). Area ratios of the three peaks in the B 1*s* region were used to determine the relative abundances B–C and B–O, indicating that B–C is dominant (73.7 ± 0.1%) in sample BDD-F (1,660 K), whereas B–O is dominant (55.2 ± 0.1%) in sample BDD-I (1,730 K). The C 1*s* peak is located at 285.2 eV, which reflects the sp^3 C–C bonds in diamond (26). A small shoulder at lower energy of 283.2 eV is observed, implying a contribution from B–C bonds (21, 26). The shoulder at higher energy suggests that some C partially bonds with B and O in diamond (26, 27). The main O 1*s* peak is located at 533.6 eV in BDD-F and shifts to lower energy in BDD-I. The shoulder at lower energies is due to a contribution of B and C with lower electronegativity than O (28, 29). The C 1*s* and O 1*s* scans for the BDD-I and BDD-F also verify the bonding configurations of B, C, and O atoms at the surface of BDD samples. The XPS data in combination with Raman spectroscopy indicate that B incorporates into the {111} diamond surface as C–B bonds at relatively low temperatures (1,660 K), while forming B–O complexes at higher temperatures (1,730 K) during diamond growth. This suggests that the ratio of C–B and B–O bonds in BDD can be tuned by controlling the B content in starting materials and experimental parameters, especially temperature.

Fig. 3*A* shows an X-ray diffraction (XRD) pattern taken from the {111} surface of BDD-F. Splitting of the (111) diffraction peaks indicates a segregated phase on the {111} surface of the BDD crystal (d_{111}, 2.0601/2.05926 Å). Optical photomicrographs of thin fragments (~10–15 μm in thickness) from the {111}

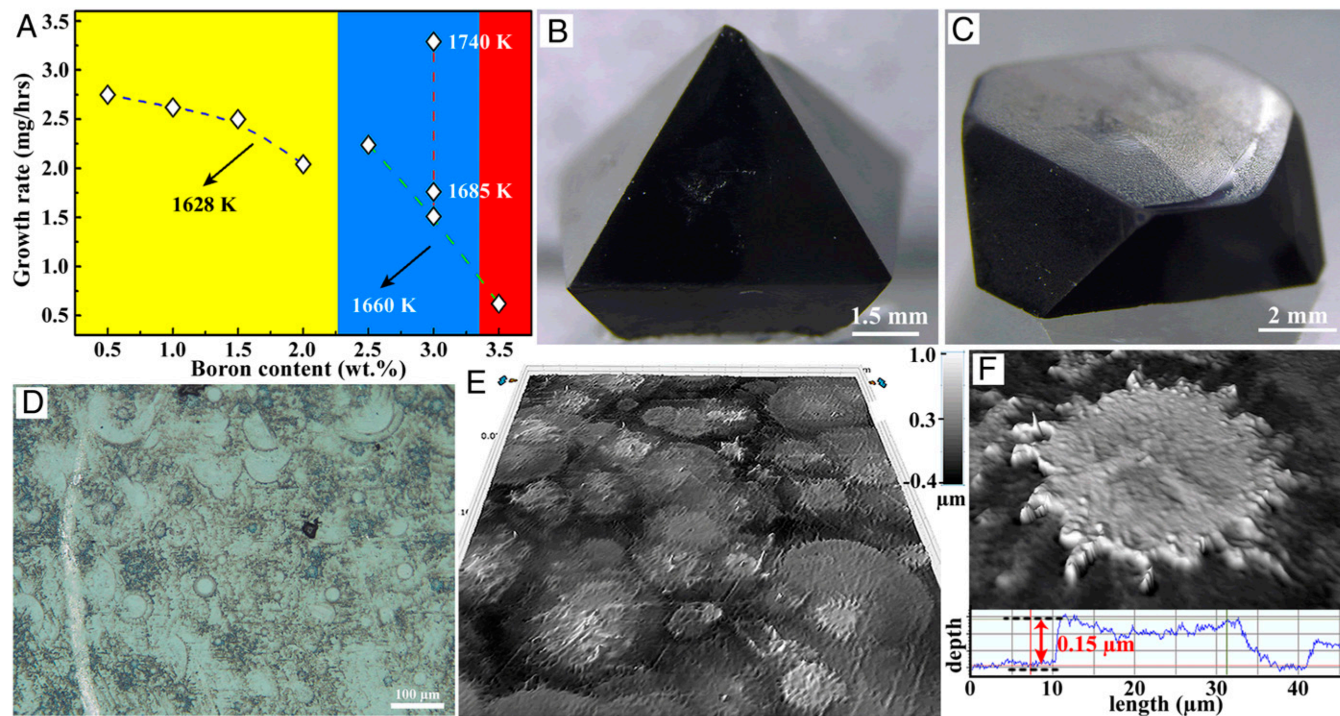

Fig. 1. HPHT synthesis of BDD single-crystal diamond. (*A*) Growth rate (mg/h) of single-crystal diamond as function of boron addition and reaction temperature (samples A–L in *SI Appendix*, Table S1). (*B*) Single-crystal BDD (sample J) before cutting and polishing with 3.0 wt % boron additive grown on a {100} substrate and (*C*) sample I grown on a {100} substrate. (*D* and *E*) The 2D and 3D optical images showing the surface morphology of the single-crystal BDD sample F. (*F*) Typical defect on the {111} surface of BDD (sample F).

APPLIED PHYSICAL SCIENCES

Fig. 2. Impurity states in BDD samples produced at different temperatures. (*A* and *B*) Raman spectra of BDD samples F and I (*SI Appendix*, Table S1), produced with 3.0 wt % B additive at 1,660 K (*B*) and 1,730 K (*A*), respectively. Shown in *Inset* are first-order longitudinal phonons (1,332 cm^{-1} for pure diamond). (*C*) XPS spectra of B 1*s*, C 1*s*, and O 1*s* core levels of diamond samples with 3.0 wt % boron addition synthesized at 1,730 K (sample I; *Top*) and 1,660 K (sample F; *Bottom*). Spectral data (red circles) are deconvolved (colored curves) by Gaussian fitting, indicating possible multibonding information for the BDD samples.

surface (Fig. 3*B*) and inner bulk (Fig. 3*C*) indicate that the inner bulk sample exhibits excellent crystallinity and is transparent with blue color, whereas the {111} surface is dark black and opaque from the high boron doping level on the diamond surface. To obtain more detailed structural characterization of the boron-rich surfaces, transmission electron microscopy (TEM) was conducted on foils taken from the as-grown {111} surface of sample BDD-F by focused ion beam (FIB). A protective coating of Pt was deposited to protect the surface cross section during the cutting and thinning process (*SI Appendix*, Figs. S5 and S6). Fig. 3*D* shows a brightfield TEM image of BDD-F, where a boron-rich layer (~15 nm thickness) is observed on the {111} surface, corroborated by the corresponding selected area electron diffraction (SAED) pattern with splitting of the (111) diffraction spots (Fig. 3*D*). Due to strain caused by lattice mismatch, the boron-rich layer shows a dark contrast in the TEM image. HRTEM images (Fig. 3*E*) of the boron-rich area show the misfit dislocation networks, accommodated by the stacking faults at the boron-rich area in Fig. 3*E*, *Inset*.

To further examine bonding characteristics in the BDD surfaces, we collected inelastic X-ray scattering (IXS) spectra at Sector 16, High-Pressure Collaborative Access Team (HPCAT) of the Advanced Photon Source (APS). *SI Appendix*, Fig. S7, shows several edges starting at 183.5 and 287.9 eV, corresponding to the characteristic K-shell ionization edges of B and C, respectively. Only σ* peaks are observed around the K edge for C, corresponding to the sp^3 bonds in diamond. K-shell ionization edges of B shows a small peak at 186.5 eV indicating the presence

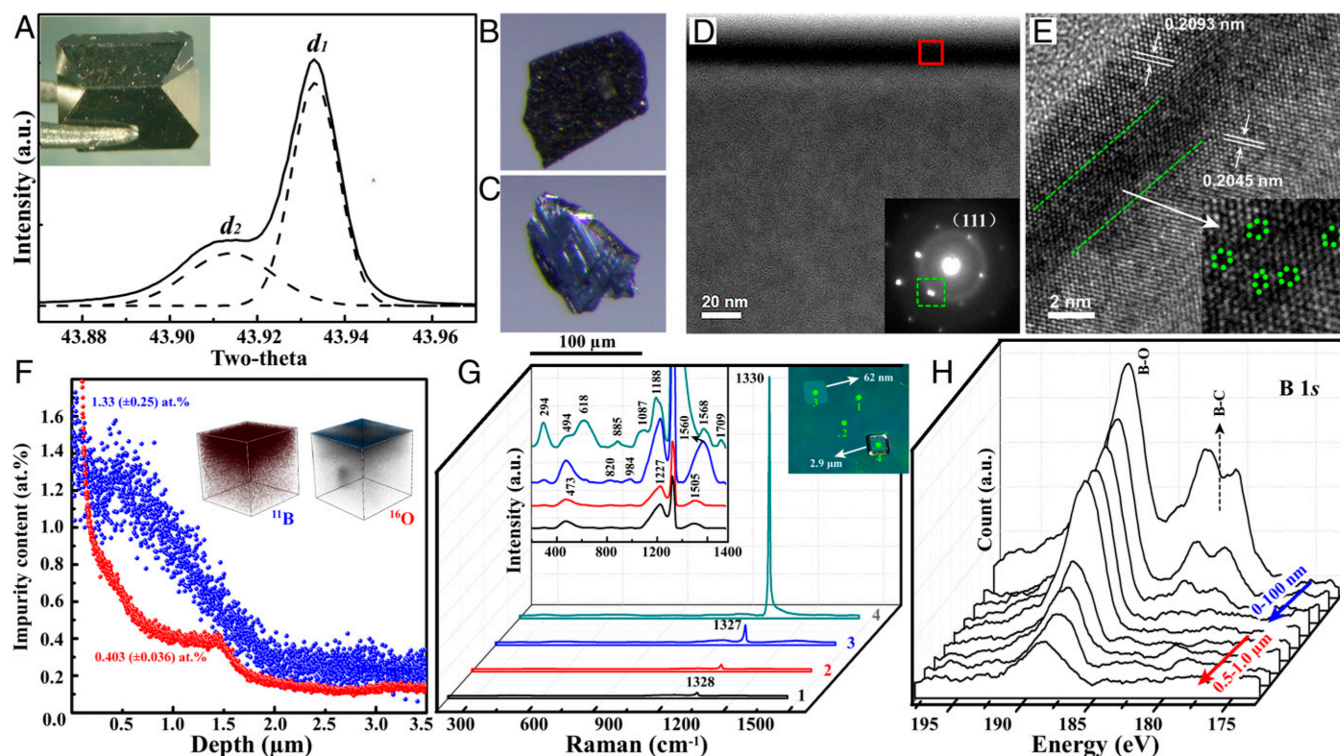

Fig. 3. Evidence for boron-rich layers on the BDD surface. (*A*) XRD pattern taken from the {111} surface of sample F produced with 3.0 wt % B at 1,660 K (*Inset*). (*B* and *C*) Optical images of two pieces taken from the surface (*B*) and inner portion (*C*) of BDD sample F before polishing. (*D*) STEM image and corresponding SAED pattern of BDD thin foil taken from the {111} plane of sample F using the FIB technique. (*E*) HRTEM image from the boron-rich area within the red box. *Inset* is the enlarged HRTEM image from a selected area between the two green dashed lines. (*F*) Impurity depth file of sample BDD-F by SIMS. *Inset* shows 3D images of ^{11}B and ^{16}O distribution in BDD-F. (*G*) Raman spectra of the BDD-F sample in four locations: two untreated parts of the crystals (spectra 1 and 2) and two treated parts of within SIMS-heated area with 62 nm and 2.9 μm depth (spectra 3 and 4), illustrated and numbered by green spots in *A*, *Inset*. *Inset* shows boron-related region. (*H*) Depth file of the B1s by XPS.

of sp^2 bonding (π*) from B impurities in the BDD, leading to the Raman peak at 1,521.6 cm^{-1} in heavily B-doped diamond (*SI Appendix*, Fig. S3).

To study the impurity concentrations and interdiffusion, secondary ion mass spectrometry (SIMS) depth file analysis was performed on the {111} surface of sample BDD-F (1,660 K) (Fig. 3*F* and *SI Appendix*, Fig. S8). Most of the boron is concentrated on the diamond {111} surface, and the maximum boron concentration reaches 1.33 ± 0.25 atomic % (∼3.99 × 10^{21} cm^{-3}) at a depth of 0.5 μm. The boron content of the interior below 2.2 μm of the BDD sample is homogeneous and low, ∼0.403 ± 0.036 atomic % (∼3.63 × 10^{20} cm^{-3}). Meanwhile, O atoms show similar diffusivity to the B impurity, but they increase in the depth range between 1.0 and 1.8 μm, where the B content decreases in the B-rich layers. Fig. 3*G* shows Raman spectra taken on the {111} diamond surface away from and within the ion-sputtered area investigated by SIMS. Within the ion-sputtered area at a depth of 62 nm, the boron-related bonds at 473 and 1,227 cm^{-1} increase, and the sp^2 bond at 1,505 cm^{-1} shifts to 1,560 cm^{-1} and also increases with increasing B content. A new series of peaks at 294, 494, 618, 885, 1,087, and 1,188 cm^{-1} are present at the depth of 2.9 μm. XPS depth profiling was carried out to study the B-rich layers of sample BDD-F. The B 1*s* scans in Fig. 3*H* reveal the evolution of boron atoms recorded at different depths through the B-rich layers toward BDD bulk, showing two regions labeled as A (0–100 nm) with blue arrow and B with red arrow (∼0.5–1.0 μm). The XPS data reveal that the B–C bonds present on the BDD surfaces disappear (i.e., are not detected by XPS spectroscopy) below a depth of 100 nm. Therefore, the presence of peaks at 294, 494, 618, 885, 1,087, and 1,188 cm^{-1} are associated with the dominant B–O bonds in diamond structure, whereas the 473 and 1,227 cm^{-1} peaks derive from the B–C bonds in BDD samples.

To investigate electrical properties of the BDD samples, we conducted four-electrode Hall effect and conductivity measurements at room temperature in the as-grown state and after removing the B-rich layers. Tables 1 and 2 summarizes the results obtained from BDD samples in different states (*SI Appendix*, Fig. S9). The BDD samples containing a high concentration of B–O bonds (BDD-I and BDD-H) show p-type semiconducting behavior with carrier concentrations of 0.271–0.570 × 10^{21} cm^{-3}. With increasing abundance of B–C bonds in diamond, a conversion from p-type to n-type conductivity is observed in these BDD samples. One sample (BDD-F) with ∼73.7 (±0.1)% B–C bonds and ∼26.3 (±0.1)% B–O bonds shows n-type semiconducting behavior with a room-temperature carrier concentration of 0.778 × 10^{21} cm^{-3} and resistivity of 0.022 Ω cm. This conductivity is almost two orders of magnitude higher than the best n-type diamond in previous studies (13, 14, 16, 18). We also measured the Seebeck coefficient in sample BDD-F, obtaining a value of −18.12 (±4.28) μV/K, providing additional evidence for the n-type semiconductivity of produced BDD materials. All of the BDD samples after polishing away the surface (BDD f–i; Tables 1 and 2) show the expected p-type semiconductivity after removal of the B-rich surfaces.

We performed low-temperature electrical measurements on the BDD samples down to 1.8 K. The samples BDD-F (before) and BDD-f (after removing boron-rich layer) behave dramatically differently at 50–1.8 K (Fig. 4*A* and *SI Appendix*, Fig. S10). We calculated the value of activation energy on the basis of a linear Arrhenius plot of the logarithm of the resistance (ln *R*)

versus the inverse temperature (T^{-1}), as shown in Fig. 4*A*, *Inset*. The as-grown BDD sample (BDD-F) shows a metallic property with low activation energy (E_g ~ 0.043 ± 0.001 meV) at low temperatures ranging from 10 to 1.8 K. After removing the as-grown surface, the resistance of sample BDD-f, dominated by B–O bonds and low boron concentrations, increases dramatically below 50 K and shows a typical semiconducting behavior (E_g ~ 10.49 ± 0.04 meV). Thus, we conclude that the shallow donor state is derived from the boron-rich layers in the as-grown {111} diamond surface.

The temperature dependence of carrier concentration and mobility for n-type BDD is shown in Fig. 4. The Hall coefficient R_H, Hall carrier density n_H and Hall mobility μ_H were obtained using the relationships $R_H = \rho_{xy}/H$, $n_H = -1/(R_H e)$, and $\mu_H = 1/(\rho n_H e)$, respectively (30). Hall resistance is remarkably linear (Fig. 4*B*, *Inset*), and the fitted R_H is negative (Fig. 4*B*), indicative of n-type carriers in BDD samples D (C16081322-20), E (C16081422-25), and F (Z15022530-17). The room-temperature carrier concentration of ~0.5–3.5 × 10^{20} cm^{-3} in the n-type BDD decreases to ~0.9–3.0 × 10^{18} cm^{-3} at 10 K (Fig. 4*C*). The carrier mobility (μ_H) of n-type BDD increases dramatically with temperature (Fig. 4*D*); for example, μ_H of BDD-E produced at 1,660 K with 2.5 wt % B additive increases from 70.85 cm^2 V^{-1} s^{-1} at room temperature up to ~1,814.8 cm^2 V^{-1} s^{-1} at temperatures

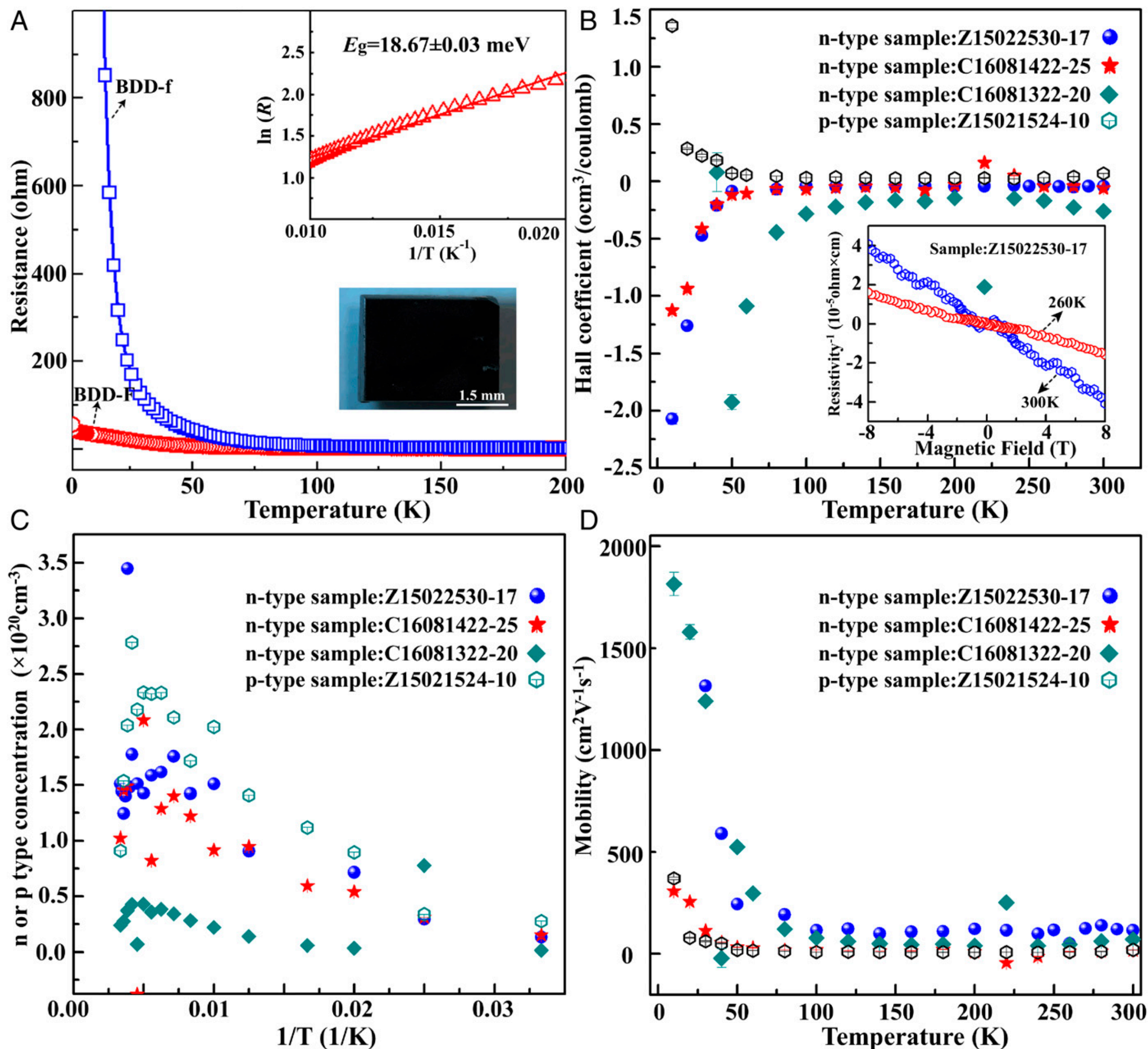

Fig. 4. Electrical properties of n-type BDD. (*A*) Resistance versus temperature curves for BDD samples with size of 3 × 3 mm and thickness of 1 mm. Two curves (red circles and blue squares) are obtained from sample F, first with the B-rich layer (BDD-F) and then after removing the B-rich layer (BBD-f), respectively (Tables 1 and 2). *Inset* shows the fitted activation energy (eV) of dopant of the BDD surface by $R(T) \propto \exp(E_g/2k_BT)$ in the range from 50 to 100 K. E_g is the activation energy, and k_B is Boltzmann's constant. The ln (*R*) as a function of T^{-1} is fitted per 50 K in the temperature range from 50 to 300 K. (*B*–*D*) The magnetoconductance for samples BDD-B, D, E, and F (synthesis conditions shown in *SI Appendix*, Table S1) at 300–10 K: (*B*) Hall coefficient as a function of temperature, (*C*) carrier concentration as a function of the reciprocal temperature, and (*D*) mobility as a function of temperature. *B*, *Inset*, shows Hall resistivity (*R*) for sample BDD-F as a function of magnetic field (±8T) at 300 and 260 K.

below 50 K. Hence, the n-type BDD maintains good electrical conductivity at low temperatures because of the high carrier mobility. Because the existence of magnetoresistance can also clearly observed in Fig. 4*B*, *Inset*, we believe that the good electrical conductivity should come from boron- and oxygen-rich surfaces in the diamond samples (Fig. 3*G*, *Inset*). Considering the low phosphorus and sulfur content of the starting materials (below 0.001%) and the fact that nitrogen and hydrogen in the as-grown surface were below the FTIR detection limit of 1 ppm (*SI Appendix*, Fig. S4*B*), we conclude that the boron–oxygen complexes are responsible for the shallow donor states in our BDD samples. Furthermore, the complex defects exhibit thermal stability to at least 1,073 K, where graphitization occurs in the bulk diamond (*SI Appendix*, Fig. S11). The source of oxygen derives from air infiltrating the powdered sources of C and B (graphite and amorphous boron) in the HPHT assembly. Whereas B and O can diffuse through the catalyst to interact with the diamond during growth, nitrogen is effectively removed by the nitrogen getter. The acid resistance of diamond minimizes the possibility that O was introduced during postsynthesis cleaning, and both SIMS (Fig. 3*F*) and XPS depth profiles (Fig. 3*H*) show that O diffused deeply into the surface (>2 μm), further suggesting that O was incorporated during HPHT diamond growth.

To further understand the shallow donors and origin of the high carrier concentration n-type semiconductivity, we performed first-principles density functional theory calculations (31, 32) to model the B/O codoped diamond. We constructed different B/O defect complexes (B_XO, X = 0–4; BO_Y, Y = 0–4) in the diamond structure based on a 64-atom 2 × 2 × 2 supercell. The optimized structures of B/O defects are shown in *SI Appendix*, Fig. S13. The C–C bond length in the optimized B/O diamond is close to 1.547 Å, the bond length in pure diamond, meaning that B and O codoping in our simulations does not significantly induce additional deformation of the lattice.

Our electronic band structure calculations show that the B/O codoped diamond is a semiconductor (*SI Appendix*, Fig. S14). The results show that the B-rich/O (B_XO) complexes, especially B_3O and B_4O defects in diamond, are clearly different from the O-doped and B/O-rich diamond, which usually exhibit deep and multiple donor levels in the band gap induced primarily by O. The calculated band structures and partial density of states (PDOS) of both B_3O- and B_4O-diamond structure are shown in Fig. 5. The B_3O complex shows a single and very shallow donor level at $E_{CBM} - 0.574$ eV, indicating an effective dopant for n-type semiconductivity. B_4O-diamond also has a dispersive and delocalized donor level which originates from the combination between the wave functions just at the B_4O defect and *p* orbitals of carbon atoms neighboring the complex defect. The shallow donor level in B_3O and B_4O complexes is due to the hybridization of B *p* and O *s p* orbitals.

We also calculated the formation energies of different systems (*SI Appendix*, Table S2). The B_3O and B_4O complexes possess the lowest formation energy of −4.27 and −6.05 eV, respectively, suggesting that the introduction of O promotes the incorporation of boron dopants into the diamond structure and that the B-rich/O complexes (B_3O and B_4O) are the most stable defects during diamond growth. There is evidence that B_4V has lower formation energy than that of isolated boron (33), which indicates boron impurities tend to aggregate with carbon vacancy to produce B_4V during crystal growth. Although dopant oxygen point defects have high formation energies in diamond, they can cross the high-energy barrier under HPHT conditions (Fig. 3 *F* and *H*). Thus, oxygen is more likely to take up the carbon vacancy surrounded by four boron atoms to overcome its high formation energy (5.31 eV for substitutional oxygen and 7.15 eV for interstitial oxygen) during diamond crystallization, leading to formation of the B_4O defect.

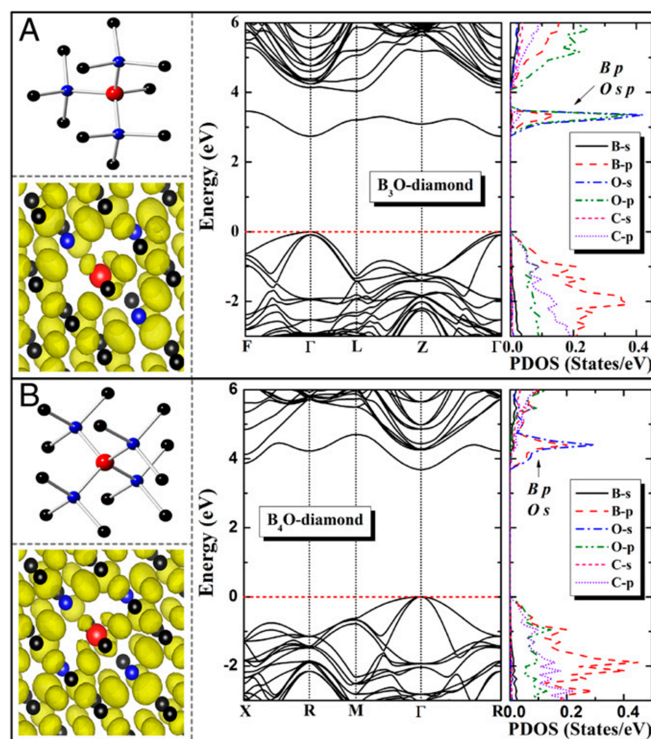

Fig. 5. Theoretical results of B–O impurity states in diamond. Optimized structures (*Upper Left*) and electron localization function isosurfaces (*Lower Left*) for (*A*) B_3O and (*B*) B_4O complexes. Only the C atoms adjacent to the B and O atoms in the structure pictures are illustrated for clarity. The blue, red, and black spheres correspond to B, O, and C atoms, respectively. The calculated band structures and PDOS for B_3O- and B_4O-diamond are shown in *A* and *B*, *Right*, respectively.

To verify our deduction and illustrate the possible synthesis pathway of B_3O- and B_4O-diamond in experiments, we calculated the formation energies of B_3V, B_4V, substitutional (O_{sub}) and interstitial O defect (O_{int}), and a carbon vacancy in diamond (*SI Appendix*, Table S2). As shown in *SI Appendix*, Table S2, the formation energies fit the relations $E^f(B_4O) < E^f(B_4V) + E^f(O_{int})$ and $E^f(B_4O) + E^f(V) < E^f(B_4V) + E^f(O_{sub})$. Therefore, B_4O complexes could be produced by the incorporation of oxygen into B_4V, which is driven by the energy reduction associated with the occupancy of vacancy by oxygen, with all carbon, boron, and oxygen atoms appropriately coordinated. Thus, n-type B/O-codoping diamond can be realized in synthesis or through annealing experiments for practical applications because of their low formation energies. The current results suggest that it is also possible to reach higher electron mobility by adjusting B/O ratio and doping concentration in B/O codoped diamond. In addition, we calculated the energy of BDD with B incorporated into different positions in the diamond {111} surface, as illustrated in *SI Appendix*, Fig. S15. The energy of the system decreases with the position of B shifting from the interior to the surface, indicating that B_3O and B_4O complexes are more likely to occur in the diamond {111} surface because B is more prone to aggregating in the surface. This result is in accord with our experiments that show n-type conductivity as measured for the diamond {111} surface. We note that this does not exclude the possibility of more complex defects in addition to those discussed.

In summary, we have synthesized boron-doped, single-crystal diamond by HPHT methods possessing a boron-rich layer 1–1.5 μm thick in the as-grown {111} surface with B–O complexes that give rise to shallow donor states for n-type semiconducting behavior with high carrier concentration (0.778×10^{21} cm^{-1}).

This structure of B–O defects (B_3O and B_4O) with low formation energy can be effectively tuned by controlling the P–T parameters during diamond crystallization, providing a route to fabricate n-type diamond semiconductors and enabling the development of future diamond-based electronic devices.

Experimental Section

HPHT Synthesis. The BDD samples were grown by TGG methods in a cubic high-pressure apparatus (SPD-6 × 1200) (*SI Appendix*, Fig. S1). High-purity graphite powders (99.99 wt % purity) and amorphous boron (99.999 wt % purity) were used as carbon and boron sources, respectively. HPHT Ib (100)- and (111)-oriented single-crystal diamond was used as substrates for diamond synthesis. Aluminum (1.0 wt %) and titanium (0.5 wt %) were added as nitrogen getter in the starting materials. Long run times up to 75 h were employed to grow large-size diamond. Synthesis temperatures were measured using a Pt-30% Rh/Pt-6%Rh thermocouple junction placed within 0.5 mm of the sample. Pressure was precalibrated at high temperatures by the graphite–diamond transition with different catalysts (Fe, Ni, and Co). After HPHT experiments, the run products were soaked in hot mixed nitric acid of H_2SO_4/HNO_3 (2:1 weight ratio) to remove the remaining graphite and metal catalyst. Diamond samples were then rinsed in water and cleaned with acetone before further characterization and electrical measurements.

Sample Characterization. The produced BDD samples were studied by a high-resolution optical microscope, SEM, TEM, and 3D optical microscopy (Bruker, ContourGT Optical Profiler) to characterize the surface defect and crystal morphology. Foils of BDD samples were prepared for TEM analysis with an FIB instrument. A custom-built confocal Raman system (458 nm excitation) and a Bomem M110 ATR FTIR spectrometer were used to evaluate boron states and concentrations, as well as H- and N-related defects in the BDD {111} surface (*SI Appendix*, Fig. S4). Each Raman spectrum was collected with a total exposure time of ∼60 s. For FTIR, an aperture of ∼150 μm square was used in the spectral range between 4,000 and 400 cm^{-1} with a spectral resolution of 1 cm^{-1}. XRD was collected on a Rigaku ATX-G. IXS spectra were collected at HPCAT, APS, beamline 16-IDD. XPS was conducted on a Thermo Scientific ESCALAB 250Xi. Two different SIMS runs were conducted. The first SIMS measurements were carried out at the Canadian Centre for Isotopic Microanalysis (CCIM), University of Alberta. At CCIM samples BDD-X and BDD-Y were analyzed (CCIM mount no. M1412). At CCIM, depth profiles were measured on a Cameca IMS-1280 multicollector ion probe with a 20-keV $^{133}C^{s}+$ ion focused to 10 μm diameter and 1 nA beam current rastered across a 45 × 45 μm area during analysis. To further investigate the potential impact of atmospheric oxygen on background SIMS measurements, a second SIMS run was conducted under high vacuum of 2×10^{-10} torr on the Physical Electronics PHI TRIFT III time-of-flight instrument at Qufu Normal University (QNU). The QNU SIMS depth profile utilized a 15-keV $^{133}Cs^{+}$ ion beam focused to 10 μm diameter and 1 nA current rastered across a 65 × 65 μm area during analysis. To calibrate boron concentration for the SIMS measurement, we measured at least four positions on the diamond surface around the SIMS-measured area by XPS and took the averaged boron values as the standard for SIMS results (*SI Appendix*, Fig. S8). Further details on SIMS measurements are provided in *SI Appendix*.

Electrical Measurement. We used the van der Pauw method for electrical transport measurements on the BDD samples, in which the effects of electrodes on the resistivity measurements can be avoided through transforming the current direction in different van der Pauw probes. Four electrodes were taped onto insulating quartz plates (5 × 5 mm in size) and placed onto the BDD sample for Hall effect and conductivity measurements. A probe station was used to test the electrical properties of the BBD samples at room temperature. To avoid the influence of inhomogeous B content in diamond, we choose {111} surfaces of produced high-quality BDD single crystals grown along (111) substrate for the Hall effect measurements. Thus, reproducible and stable Hall signal could be obtained for the electrical characterization. The electrical characteristics were measured with an electronic transport properties measuring system (East Changing ET 9000 Series). The resistivity measurement was carried out at room temperature (300 K) and normal humidity level (40% RH). We further characterized the electrical properties of BDD samples by investigating the temperature dependence of the resistance using a standard four-probe method in a PPMS (Quantum Design) in the range of 300–1.8 K. The Seebeck coefficients S were measured by the four-point probe method using a thermoelectric measurement system. The Hall resistivity ρ_{xy} was measured by a four-point contact method by sweeping magnetic fields from −8T to 8T. The Hall coefficient R_H, Hall carrier density n_H, and Hall mobility μ_H were obtained using the relationships of $R_H = \rho_{xy}/H$, $n_H = -1/(R_H e)$, and $\mu_H = 1/(\rho n_H e)$, respectively.

First-Principles Calculations. All calculations were performed using the projector augmented wave method and the generalized gradient approximation with the Perdew–Burke–Ernzerhof functional (34), as implemented in the Vienna Ab-initio simulation package (35, 36). The plane-wave kinetic energy cutoffs of 550 eV and the Monkhorst–Pack *k*-point meshes of 8 × 8 × 8 were chosen to ensure that all of the structures converged to better than 10^{-5} eV. The structure optimizations were performed for all configurations with the lattice constants and all atoms relaxed until the Hellmann–Feynman forces were less than 0.01 eV/Å. We constructed different B/O defect complexes (B rich/O and B/O rich) based on a 64-atom 2 × 2 × 2 supercell. Because the boron and oxygen defects in diamond usually exist in the type of substitution, we replaced adjacent carbon atoms in the supercell by one boron and one, two, three, or four oxygen atoms, corresponding to BO-, BO_2-, BO_3-, and BO_4-diamond, respectively. Similarly, B_2O-, B_3O-, and B_4O-diamond are constructed to illustrate the effects of the number of B and O atoms on the electronic structures of diamond. Although our computational model agrees well with the experimental observations on n-type conduction, our supercell containing B–O complex assumes a perfect crystal with ordered defects, which should be tested in future computational studies of n-type diamond with B–O complexes.

ACKNOWLEDGMENTS. The authors acknowledge help of Dr. J. G. Guo for LT-resistance measurements at Rice University and Prof. X. P. Jia and H. A. Ma for sample preparation and Hall effect measurements at Jilin University. This work was supported by the National Science Foundation of China Grant 11804184 (to X.C.) and by awards from the US National Science Foundation (NSF) Grant DMR-1508577, the David and Lucile Packard Foundation, the Alexander von Humboldt Foundation, and the Department of Energy (DOE) through the Capital/DOE Alliance Center (S.D.J.). D.J.S. acknowledges support from the DOE, Basic Energy Sciences, Grant DE-SC0019114. This work made use of the TEM, SEM, and XPS facilities of Northwestern University Atomic and Nanoscale Characterization Experimental Center, which has received support from the Soft and Hybrid Nanotechnology Experimental Resource (NSF Grant ECCS-1542205), the Materials Research Science and Engineering Centers program (NSF Grant DMR-1121262) at the Materials Research Center, the International Institute for Nanotechnology (IIN), the Keck Foundation, and the State of Illinois through the IIN. The FIB at Bayerisches Geoinstitut, University of Bayreuth, Germany, was financed by DFG Grant INST 91/315-1 FUGG. IXS measurements were performed at HPCAT (Sector 16), APS, Argonne National Laboratory (ANL). HPCAT operations are supported by DOE–National Nuclear Security Administration under Award DE-NA0001974, with partial instrumentation funding by NSF. The APS is a DOE Office of Science User Facility operated by ANL under Contract DE-AC02-06CH11357. The calculations were performed in the High Performance Computing Center of Qufu Normal University and Quest high performance computing facility at Northwestern University.

1. Koizumi S, Watanabe K, Hasegawa M, Kanda H (2001) Ultraviolet emission from a diamond pn junction. *Science* 292:1899–1901.
2. Isberg J, et al. (2002) High carrier mobility in single-crystal plasma-deposited diamond. *Science* 297:1670–1672.
3. Nebel CE (2013) Valleytronics: Electrons dance in diamond. *Nat Mater* 12:690–691.
4. Umezawa H, Nagase M, Kato Y, Shikata S-i (2012) High temperature application of diamond power device. *Diamond Relat Mater* 24:201–205.
5. Pickett WE (1994) Negative electron affinity and low work function surface: Cesium on oxygenated diamond (100). *Phys Rev Lett* 73:1664–1667.
6. May PW (2008) Materials science. The new diamond age? *Science* 319:1490–1491.
7. Laks DB, Van de Walle CG, Neumark GF, Pantelides ST (1991) Role of native defects in wide-band-gap semiconductors. *Phys Rev Lett* 66:648–651.
8. Kajihara SA, Antonelli A, Bernholc J, Car R (1991) Nitrogen and potential n-type dopants in diamond. *Phys Rev Lett* 66:2010–2013.
9. Sakaguchi I, et al. (1999) Sulfur: A donor dopant forn-type diamond semiconductors. *Phys Rev B Condens Matter Mater Phys* 60:2139–2141.
10. Farrer RG (1969) On the substitutional nitrogen donor in diamond. *Solid State Commun* 7:685–688.
11. Li BB, Tosin MC, Peterlevitz AC, Baranauskas V (1998) Measurement of the substitutional nitrogen activation energy in diamond films. *Appl Phys Lett* 73:812–814.
12. Saada D, Adler J, Kalish R (2000) Sulfur: A potential donor in diamond. *Appl Phys Lett* 77:878–879.
13. Kalish R, Reznik A, Uzan-Saguy C, Cytermann C (2000) Is sulfur a donor in diamond? *Appl Phys Lett* 76:757–759.
14. Koizumi S, Kamo M, Sato Y, Ozaki H, Inuzuka T (1997) Growth and characterization of phosphorous doped {111} homoepitaxial diamond thin films. *Appl Phys Lett* 71:1065–1067.
15. Kato H, Ogura M, Makino T, Takeuchi D, Yamasaki S (2016) N-type control of single-crystal diamond films by ultra-lightly phosphorus doping. *Appl Phys Lett* 109:142102.

16. Jones R, Lowther JE, Goss J (1996) Limitations to n-type doping in diamond: The phosphorus-vacancy complex. *Appl Phys Lett* 69:2489–2491.
17. Miyazaki T, Okushi H, Uda T (2002) Shallow donor state due to nitrogen-hydrogen complex in diamond. *Phys Rev Lett* 88:066402.
18. Teukam Z, et al. (2003) Shallow donors with high n-type electrical conductivity in homoepitaxial deuterated boron-doped diamond layers. *Nat Mater* 2:482–486.
19. Sque SJ, Jones R, Goss JP, Briddon PR (2004) Shallow donors in diamond: Chalcogens, pnictogens, and their hydrogen complexes. *Phys Rev Lett* 92:017402.
20. Sidorov VA, Ekimov EA (2010) Superconductivity in diamond. *Diamond Relat Mater* 19:351–357.
21. Ci L, et al. (2010) Atomic layers of hybridized boron nitride and graphene domains. *Nat Mater* 9:430–435.
22. Liu G, Yin LC, Niu P, Jiao W, Cheng HM (2013) Visible-light-responsive β-rhombohedral boron photocatalysts. *Angew Chem Int Ed Engl* 52:6242–6245.
23. Paul R, Voevodin AA, Zemlyanov D, Roy AK, Fisher TS (2012) Microwave-assisted surface synthesis of a boron-carbon-nitrogen foam and its desorption enthalpy. *Adv Funct Mater* 22:3682–3690.
24. Vincent H, Vincent C, Scharff JP, Mourichoux H, Bouix J (1992) Thermodynamic and experimental conditions for the fabrication of a boron carbide layer on high-modulus carbon fiber surfaces by RCVD. *Carbon* 30:495–505.
25. Cermignani W, Paulson TE, Onneby C, Pantano CG (1995) Synthesis and characterization of boron-doped carbons. *Carbon* 33:367–374.
26. Liu X, et al. (2016) Ultrahard stitching of nanotwinned diamond and cubic boron nitride in C_2-BN composite. *Sci Rep* 6:30518.
27. Zhao G, et al. (2011) Sulfonated graphene for persistent aromatic pollutant management. *Adv Mater* 23:3959–3963.
28. Zhou Z, et al. (2014) Nitrogen- and oxygen-containing activated carbon nanotubes with improved capacitive properties. *RSC Adv* 4:5524–5530.
29. Honma T, Benino Y, Komatsu T, Sato R, Dimitrov V (2002) Correlation among electronic polarisability, optical basicity, interaction parameter and XPS spectra of Bi_2O_3-B_2O_3 glasses. *Phys Chem Glasses* 43:32–40.
30. Ginting D, et al. (2017) High thermoelectric performance due to nano-inclusions and randomly distributed interface potentials in N-type $(PbTe_{0.93-x}Se_{0.07}Cl_x)_{0.93}(PbS)_{0.07}$ composites. *J Mater Chem A Mater Energy Sustain* 5:13535–13543.
31. Kohn W, Sham LJ (1965) Self-consistent equations including exchange and correlation effects. *Phys Rev* 140:1133–1138.
32. Hohenberg P, Kohn W (1964) Inhomogeneous electron gas. *Phys Rev* 136:864–871.
33. Goss JP, Briddon PR (2006) Theory of boron aggregates in diamond: First-principles calculations. *Phys Rev B Condens Matter Mater Phys* 73:085204.
34. Perdew JP, Burke K, Ernzerhof M (1996) Generalized gradient approximation made simple. *Phys Rev Lett* 77:3865–3868.
35. Kresse G, Furthmüller J (1996) Efficient iterative schemes for ab initio total-energy calculations using a plane-wave basis set. *Phys Rev B Condens Matter* 54:11169–11186.
36. Kresse G, Furthmüller J (1996) Efficiency of ab-initio total energy calculations for metals and semiconductors using a plane-wave basis set. *Comput Mater Sci* 6:15–50.